Low-temperature $B2$ ordering and magnetic properties of $Fe_{100-x}Rh_x$ films on bcc alloys

S. Yamada,[1,2,*] K. Tanikawa,[2] J. Hirayama,[1,2] T. Kanashima,[1] T. Taniyama,[3] and K. Hamaya[1,2,†]

[1]*Graduate School of Engineering Science, Osaka University, Toyonaka 560-8531, Japan*

[2]*Department of Electronics, Kyushu University, 744 Motooka, Fukuoka 819-0395, Japan*

[3]*Materials and Structures Laboratory, Tokyo Institute of Technology, 4259 Nagatsuta, Midori-ku, Yokohama 226-8503, Japan*

(Received 16 June 2015; revised manuscript received 8 August 2015; published 10 September 2015)

$B2$-ordered $Fe_{100-x}Rh_x$ alloys, which exhibit a first-order magnetic phase transition from an antiferromagnetic state to a ferromagnetic one at around 350 K, have so far been formed by high-temperature heat treatments above 600 °C. Here we demonstrate low-temperature (200 °C) growth of $B2$-ordered $Fe_{100-x}Rh_x$ films on body-centered-cubic (bcc) alloys. By using molecular beam epitaxy with an insertion of $D0_3$-ordered Fe_3Si buffer layers, which have good atomic arrangement matching with $Fe_{100-x}Rh_x$ along ⟨111⟩, $B2$-ordered $Fe_{100-x}Rh_x$ films having a sharp magnetic phase transition can be obtained at 200 °C even in as-grown conditions. We find that the disordered structures are mainly derived from the lattice strain in the $Fe_{100-x}Rh_x$ films due to the lattice mismatch between $Fe_{100-x}Rh_x$ and the buffer layers. We discuss the role of heat treatments and other buffer structures on the $B2$-ordering and magnetic properties for $Fe_{100-x}Rh_x$ films.

DOI: 10.1103/PhysRevB.92.094416 PACS number(s): 75.50.Bb, 75.70.Ak, 81.15.Hi

I. INTRODUCTION

$Fe_{100-x}Rh_x$ alloys with a $B2$-ordered structure exhibit a first-order magnetic phase transition from an antiferromagnetic (AFM) state to a ferromagnetic (FM) one at around 350 K with a temperature hysteresis width of ∼10 K between heating and cooling cycles [1]. This phase transition is accompanied by a unit cell volume expansion of ∼1% [2], a significant reduction in resistivity [3], and enormous magnetoresistance [4,5]. Due to the unique features, various applications such as spin-valve devices [6], micro-electrical-chemical systems [7], thermal-assisted magnetic recording (TAMR) [8], and AFM memory resistors [9] have been reported. One of the important issues for the applications is to manipulate the AFM-FM phase transition of $Fe_{100-x}Rh_x$ alloys. Up to now, it has been induced by a spin-polarized current [10], an electric field [11], a lattice strain accompanied by the structural phase transition [12], and laser heating [13].

Over the past more than 50 years, many studies of structural and magnetic properties for bulk [3–5,14–18] and thin-film [6–13,19–37] $Fe_{100-x}Rh_x$ have been reported. To observe a sharp AFM-FM phase transition, the formation of $B2$-ordered $Fe_{100-x}Rh_x$ is required. Although many groups achieved the formation of $B2$-ordered $Fe_{100-x}Rh_x$, common requirements in almost all studies were high-temperature heat treatments above 600 °C [3–37]. However, for applications such as in spin-valve devices [6] and TAMR [8], the high-temperature heat treatments can induce atomic interdiffusion at the interfaces, giving rise to degradation of the structural and magnetic properties. In addition, the high-temperature heat treatments are incompatible with conventional semiconductor technologies. Furthermore, the softening temperature of aluminum-alloy or glass substrates used in the current hard disk drives is much lower than the $B2$-ordering temperature. From a viewpoint of practical applications, reduction in the $B2$-ordering temperature should be strongly explored, but almost no one has ever approached the low-temperature $B2$ ordering of $Fe_{100-x}Rh_x$ alloys.

For the low-temperature structural ordering of body-centered-cubic (bcc) ordered alloys, we focus on molecular beam epitaxy (MBE). To date, we have demonstrated epitaxial growth of some kinds of ordered Heusler alloys on Ge at low growth temperatures (T_G) below 200 °C [38–40], where Heusler alloys are one of the candidate materials for FM electrodes in high-performance spintronic devices [41–44]. Although one has generally needed high-temperature heat treatments above 500 °C, our low-temperature MBE technique can achieve a relatively high degree of the structural ordering even in as-grown conditions [39]. We now speculate that precise control of the chemical composition in films using Knudsen cells and certain special conditions on the crystal structure between Heusler alloys and Ge can largely reduce the ordering temperature [39,40]. As described later in detail, since $B2$-ordered $Fe_{100-x}Rh_x$ can also satisfy the special conditions as well as Heusler alloys, low-temperature $B2$ ordering of $Fe_{100-x}Rh_x$ can be expected by using MBE techniques.

In this article, we explore low-temperature $B2$ ordering of $Fe_{100-x}Rh_x$ films by using MBE. $B2$-ordered $Fe_{100-x}Rh_x$ films are obtained at T_G of 200 °C when the films are grown on top of $D0_3$-Fe_3Si layers, which have good atomic arrangement matching with $Fe_{100-x}Rh_x$ along ⟨111⟩. We find that the disordered structures are mainly derived from the lattice strain in the $Fe_{100-x}Rh_x$ films due to lattice mismatch between $Fe_{100-x}Rh_x$ and $D0_3$-Fe_3Si. The role of heat treatments and other buffer structures on the $B2$ ordering and the magnetic properties of $Fe_{100-x}Rh_x$ films is discussed.

II. CONCEPT FOR LOW-TEMPERATURE $B2$ ORDERING

We explain a concept for forming $B2$-ordered $Fe_{100-x}Rh_x$ films at low temperature. The crystal structures of $B2$-ordered $Fe_{100-x}Rh_x$ (top), $D0_3$-ordered Fe_3Si (middle), and Ge (bottom) are shown in Fig. 1(a). $D0_3$-ordered Fe_3Si, which is one of ferromagnetic Heusler alloys, and Ge have bcc and diamond crystal structures, respectively. The lattice mismatch

*yamada@ee.es.osaka-u.ac.jp
†hamaya@ee.es.osaka-u.ac.jp

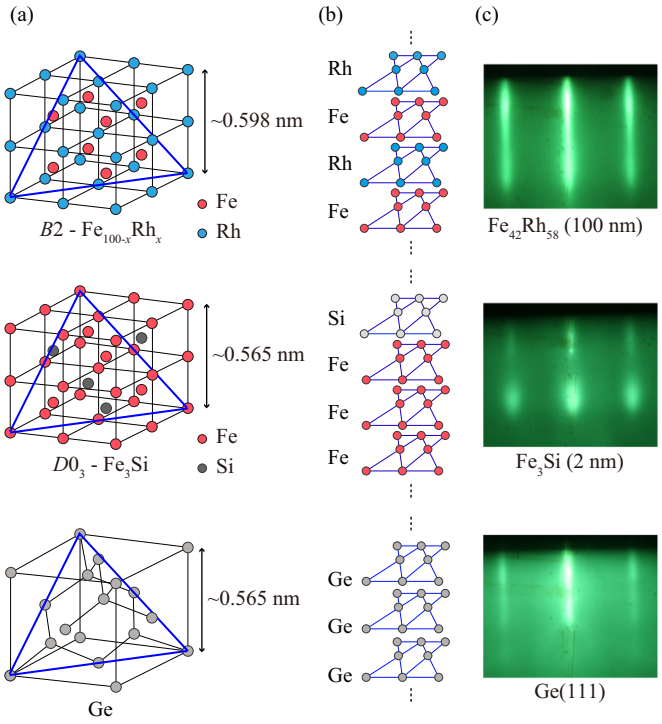

FIG. 1. (Color online) (a) Crystal structure of $B2$-ordered $Fe_{100-x}Rh_x$ (top), $D0_3$-ordered Fe_3Si (middle), and Ge (bottom). (b) Atomic arrangements of $B2$-ordered $Fe_{100-x}Rh_x$, $D0_3$-ordered Fe_3Si, and Ge along $\langle 111\rangle$. (c) RHEED patterns of the surface for $Fe_{42}Rh_{58}$ layer, Fe_3Si buffer layer, and the Ge(111) substrate, observed along $[\bar{2}11]$ azimuth.

of $D0_3$-ordered Fe_3Si and Ge is almost zero, and good atomic arrangement matching is seen along $\langle 111\rangle$ (see triangles in the figure) [38]. $D0_3$-ordered Fe_3Si has a periodic stacking structure consisting of three Fe atomic layers and one Si atomic layer along $\langle 111\rangle$, as shown in the center of Fig. 1(b). Utilizing the special conditions, we have demonstrated epitaxial growth of $D0_3$-ordered Fe_3Si films on Ge(111) at low T_G below 200 °C even in as-grown conditions [38–40]. The special conditions enabled us to achieve high-quality epitaxial growth of single-crystalline Ge films on top of $D0_3$-ordered Fe_3Si at relatively low T_G [45,46]. Interestingly, even though there is ∼4% lattice mismatch between Ge and Si, we also demonstrated epitaxial growth of strain-free Ge layers on a Si substrate using an Fe_3Si insertion layer [46], meaning that bcc alloys, which have the good atomic arrangement matching with Ge along $\langle 111\rangle$, can become buffer layers for high-quality Ge films. Here we note that $B2$-ordered $Fe_{100-x}Rh_x$ can also satisfy the special conditions. Although there exists ∼6% lattice mismatch between $B2$-ordered $Fe_{100-x}Rh_x$ and $D0_3$-ordered Fe_3Si, $B2$-ordered $Fe_{100-x}Rh_x$ consists of alternately stacked atomic layers of Fe and Rh along $\langle 111\rangle$, as shown in the top of Fig. 1(b). Of course, good atomic arrangement matching is seen along $\langle 111\rangle$ [see triangles in Fig. 1(a)]. Therefore, low-temperature $B2$ ordering of $Fe_{100-x}Rh_x$ can be expected on $D0_3$-Fe_3Si as a bcc-alloy buffer layer by using MBE techniques.

III. RESULTS AND DISCUSSION

A. $B2$ ordering at 200 °C

$Fe_{100-x}Rh_x$ films ($x = 53$, 54, and 58) were grown on Ge(111) substrates with a 2-nm-thick Fe_3Si buffer layer. The detailed procedure for the surface cleaning of the substrates was described in our previous studies [38–40]. During the growth, we performed *in situ* reflection high-energy electron diffraction (RHEED) observations. After we confirmed that the RHEED patterns of the Ge(111) surface indicated an atomically smooth surface [the bottom of Fig. 1(c)], we grew the 2-nm-thick Fe_3Si buffer layer at room temperature (RT) [40]. The growth rate of Fe_3Si was ∼2.3 nm/min and the cell temperature of Fe and Si was ∼1260 and ∼1380 °C, respectively. Although the surface for the Fe_3Si buffer layer is slightly rough, epitaxial growth is indicated [the middle of Fig. 1(c)]. On top of the surface, we grew a 100-nm-thick $Fe_{100-x}Rh_x$ layer at T_G of 200 °C by co-evaporating Fe and Rh using Knudsen cells. The growth rate of $Fe_{100-x}Rh_x$ was ∼2.0 nm/min and the cell temperature of Fe and Rh was ∼1815 and ∼1215 °C, respectively. As a result, the RHEED pattern of the $Fe_{100-x}Rh_x$ surface showed clear streaks [the top of Fig. 1(c)], indicating good two-dimensional epitaxial growth.

A cross-sectional transmission electron microscope (TEM) image of the grown $Fe_{42}Rh_{58}/Fe_3Si$ bilayer on Ge(111) is displayed in Fig. 2(a). An epitaxial $Fe_{42}Rh_{58}$ layer is obtained on Ge(111) through the Fe_3Si buffer layer and no interlayer is observed near the interface. We can see some Moiré-like patterns in the $Fe_{42}Rh_{58}$ layer. We speculate that the Moiré-like patterns originate from the lattice strain due to the lattice mismatch of ∼6% between $Fe_{42}Rh_{58}$ and Fe_3Si. The $\theta-2\theta$ x-ray diffraction (XRD) pattern of the $Fe_{42}Rh_{58}(100\text{ nm})/D0_3 - Fe_3Si(2\text{ nm})/Ge(111)$ is shown in Fig. 2(b). Since there is almost no lattice mismatch between $Fe_3Si(111)$ and Ge(111) and the thickness of the Fe_3Si buffer layer is very thin, the diffraction peaks originating from Fe_3Si are overlapped with those of Ge [39]. Note that clear (111) and (222) diffraction peaks of $B2$-ordered $Fe_{100-x}Rh_x$ are seen at 2θ of ∼53° and ∼126°, respectively, indicating the formation of a $B2$-ordered $Fe_{42}Rh_{58}$ film. The lattice constant of the $Fe_{42}Rh_{58}$ film estimated from the diffraction peaks at 2θ of ∼53° and ∼126° was ∼0.299 and ∼0.300 nm, respectively, almost equivalent to that of bulk $Fe_{100-x}Rh_x$ (∼0.299 nm) [14]. A weak diffraction peak at 2θ of ∼45° is due to the presence of a disordered face-centered-cubic (fcc) phase (γ-FeRh) [30]. We infer that the lattice mismatch between $Fe_{100-x}Rh_x$ and Fe_3Si induced the interfacial stress, leading to the formation of a disordered fcc phase in the $Fe_{42}Rh_{58}$ film [30,31]. Also, very weak diffraction peaks due to the formation of Fe-based germinide compounds are observed at 2θ of ∼35° and ∼75°. We speculate that they were formed by an interdiffusion at the interface between Fe_3Si and Ge(111) during the growth of FeRh due to an increase in a substrate temperature from RT to 200 °C. Note that there are no diffraction peaks originating from an interdiffusion between $Fe_{42}Rh_{58}$ and Ge(111), meaning that $B2$-ordered $Fe_{42}Rh_{58}$ films were grown on top of a $D0_3$-Fe_3Si buffer layer with no intermixing. Thus, we obtained $B2$-ordered $Fe_{42}Rh_{58}$ films at T_G of 200 °C, where the $B2$-ordering temperature is much lower than those reported so far [3–37].

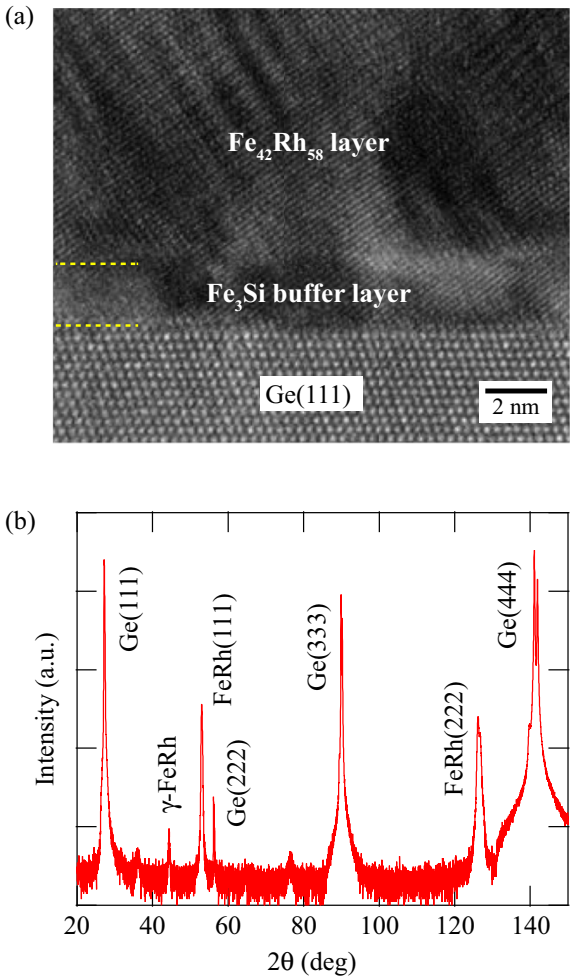

FIG. 2. (Color online) (a) Cross-sectional TEM image of $Fe_{42}Rh_{58}$(100 nm)/$D0_3$-Fe_3Si(2 nm)/Ge(111) near the interfaces. (b) θ-2θ XRD pattern of the $Fe_{42}Rh_{58}$(100 nm)/$D0_3$-Fe_3Si(2 nm)/Ge(111).

Magnetic properties were measured with a vibrating sample magnetometer at various temperatures ranging from 100 to 400 K using a physical property measurement system (Quantum Design, PPMS). Figure 3 shows the temperature dependence of magnetization (M-T curves) of $Fe_{100-x}Rh_x$(100 nm)/$D0_3$-Fe_3Si(2 nm)/Ge(111) for x of 53, 54, and 58 during the heating and cooling cycles. During the measurements, a magnetic field of 0.1 T was applied parallel to the film plane and the background data from the Ge substrate was subtracted from the raw data. Since the thickness of the Fe_3Si buffer layer is very thin, the magnetization originating from the Fe_3Si buffer layer can be neglected. This figure clearly shows that all the films have a first-order magnetic phase transition from the AFM state to the FM one above 300 K. With increasing x, the AFM-FM phase transition temperature shifts to a high-temperature region and a temperature hysteresis width of the AFM-FM phase transition becomes small. We have not yet clarified the reason for the difference in the chemical composition of $B2$-ordered $Fe_{100-x}Rh_x$ alloys, where the AFM-FM phase transition was seen, between our thin-film samples ($x = 53 \sim 58$) and bulk ones reported ($x = 48 \sim 54$)

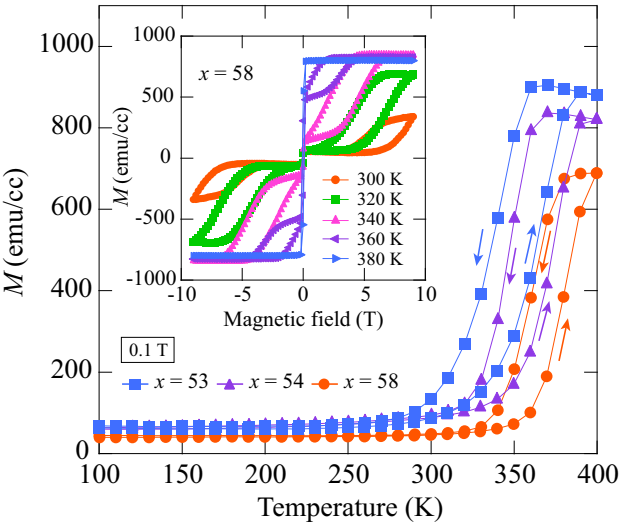

FIG. 3. (Color online) M-T curves of $Fe_{100-x}Rh_x$(100 nm)/$D0_3$-Fe_3Si(2 nm)/Ge(111) for $x = 53$, 54, and 58 during the heating and cooling cycles. The inset shows M-H curves of the $Fe_{42}Rh_{58}$ (100 nm)/$D0_3$-Fe_3Si(2 nm)/Ge(111) measured at various temperatures ranging from 300 to 380 K during the heating cycle.

[14]. It should be noted that, even for thin-film samples grown at T_G of 200 °C, the values of the magnetization in a low-temperature regime for x of 58 are very low (~40 emu/cc), which is comparable to that of the thin-film sample annealed at 600 °C reported [26].

We also explored the effect of thickness on the magnetic properties for $Fe_{42}Rh_{58}$ films for the thickness of 25, 50, and 100 nm. Although all the films showed an AFM-FM phase transition above 300 K, the AFM-FM phase transition was slightly smeared and temperature hysteresis width of the AFM-FM phase transition was broad with decreasing the film thickness. In particular, the values of the magnetization in a low-temperature regime for the 25-nm-thick $Fe_{42}Rh_{58}$ film were relatively large (~180 emu/cc), indicating that some FM states were stable with decreasing the film thickness [30]. From these results, we understood that disordered structures are mainly derived from the lattice strain in the $Fe_{42}Rh_{58}$ film due to the lattice mismatch between $Fe_{42}Rh_{58}$ and Fe_3Si [30,32].

The inset of Fig. 3 shows field-dependent magnetization (M-H curves) of the $Fe_{42}Rh_{58}$(100 nm)/$D0_3$-Fe_3Si(2 nm)/Ge(111) measured at various temperatures ranging from 300 to 380 K, which correspond to the magnetization changes with temperatures during the heating cycle. The M-H curve at 380 K shows a clear FM behavior while those ranging from 300 to 360 K show a magnetic-field-induced AFM-FM phase transition, which is a typical characteristic of a first-order magnetic phase transition of $B2$-ordered $Fe_{100-x}Rh_x$. This feature also assures that the low-temperature-grown $Fe_{42}Rh_{58}$ film consists of $B2$-ordered structures.

B. Effect of bcc-alloy buffers

We examine the effect of an insertion of $D0_3$-Fe_3Si on the growth of $Fe_{42}Rh_{58}$ films. Interestingly, even for the growth without $D0_3$-Fe_3Si, two-dimensional epitaxial growth of the

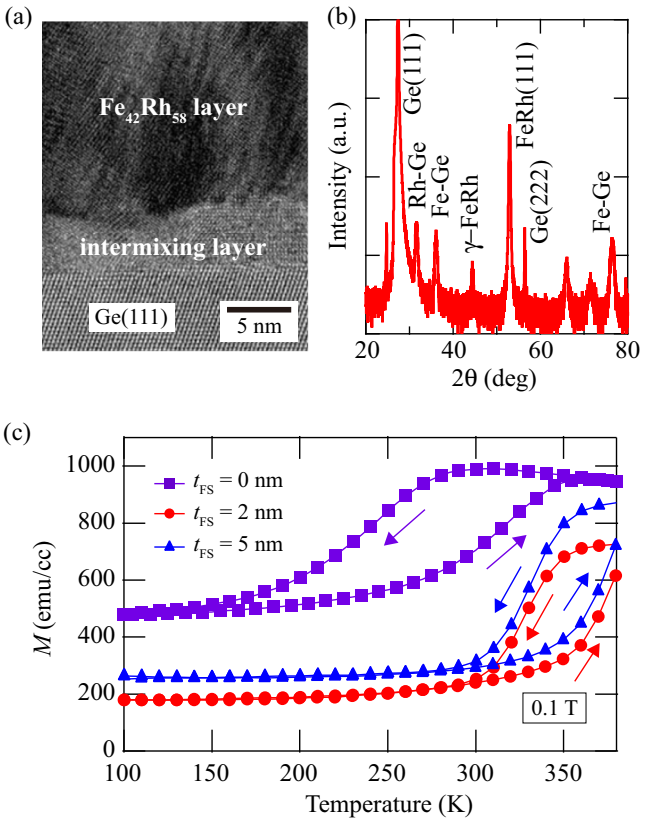

FIG. 4. (Color online) (a) Cross-sectional TEM image of $Fe_{42}Rh_{58}$(25 nm)/Ge(111) near the interface. (b) θ-2θ XRD pattern of the $Fe_{42}Rh_{58}$(25 nm)/Ge(111). (c) M-T curves of $Fe_{42}Rh_{58}$(25 nm)/$D0_3$-Fe_3Si/Ge(111), where t_{FS} is 0, 2, and 5 nm.

$Fe_{42}Rh_{58}$ films was observed from *in situ* RHEED patterns (not shown). However, as shown in Fig. 4(a), we can observe an intermixing layer with a thickness of ∼4 nm near the interface even if we reduce T_G down to RT. From energy-dispersive x-ray spectroscopy measurements, a large number of Rh and Ge atoms were detected in the intermixing layer, indicating that germinidation reaction occurred during the growth and that Rh-based germinide compounds were mainly formed at the interface even for the RT growth. The θ-2θ XRD pattern of the sample is shown in Fig. 4(b). In addition to a diffraction peak corresponding to FeRh(111), some diffraction peaks arising from the formation of other phases such as Rh- and Fe-based germinide compounds are observed. Namely, we found that the interfacial reactions cannot be prevented without $D0_3$-Fe_3Si. Figure 4(c) shows the M-T curve of $Fe_{42}Rh_{58}$(25 nm)/Ge(111), together with those of $Fe_{42}Rh_{58}$(25 nm)/$D0_3$-Fe_3Si/Ge(111), where the thickness of the inserted Fe_3Si buffer layer (t_{FS}) is 2 and 5 nm. Note that the samples used here are 25-nm-thick RT-grown films and the quality of the films is different from that grown at T_G of 200 °C, as described in Sec. III A. Compared with the samples for t_{FS} of 2 and 5 nm, the M-T curve for the $Fe_{42}Rh_{58}$(25 nm)/Ge(111) (t_{FS} = 0 nm) clearly includes the broad temperature hysteresis of the AFM-FM phase transition and the magnetization in a low-temperature regime for the 25-nm-thick $Fe_{42}Rh_{58}$ film shows large values (∼500 emu/cc), meaning the presence of a relatively large

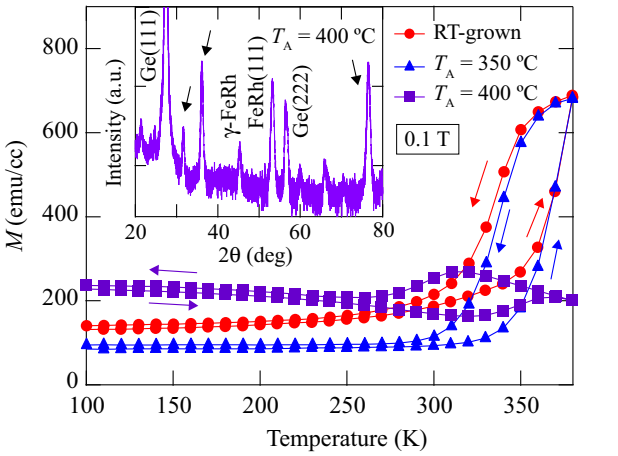

FIG. 5. (Color online) M-T curves of RT-grown $Fe_{42}Rh_{58}$ (100 nm)/$D0_3$-Fe_3Si(2 nm)/Ge(111) before and after the postannealing. The inset shows a θ-2θ XRD pattern of the sample annealed at T_A of 400 °C.

number of disordered structures in the $Fe_{42}Rh_{58}$ film. Also, the AFM-FM phase transition temperature significantly shifts down to ∼150 K. We infer that the germinidation reaction induced the deviation of the chemical composition in the $Fe_{42}Rh_{58}$ film, giving rise to the degradation of the structural and magnetic properties. On the other hand, the shape of the M-T curve for t_{FS} of 2 nm is almost equivalent to that for t_{FS} of 5 nm. With increasing t_{FS} from 2 to 5 nm, the increase in the magnetization in the low-temperature regime is seen, caused by the increase in the ratio of t_{FS} to the total thickness. From these results, we conclude that the Fe_3Si buffer layer, shown in Fig. 2(a), can act as a protection layer for preventing the diffusion of Ge atoms into the $Fe_{42}Rh_{58}$ layer during the growth even though t_{FS} is only 2 nm [47].

C. Effect of heat treatments

We investigate the role of heat treatments on the structural ordering for $Fe_{42}Rh_{58}$ films. Figure 5 shows the M-T curves of RT-grown $Fe_{42}Rh_{58}$(100 nm)/$D0_3$-Fe_3Si(2 nm)/Ge(111) before and after the postannealing. First, we compare the RT-grown $Fe_{42}Rh_{58}$/$D0_3$-Fe_3Si/Ge(111) with the 200 °C–grown one. As seen in Fig. 5 (red circles), the M-T curve of the RT-grown $Fe_{42}Rh_{58}$/$D0_3$-Fe_3Si/Ge(111) shows an AFM-FM phase transition and a small temperature hysteresis width. However, the values of the magnetization in a low-temperature regime are relatively high (∼140 emu/cc) and a temperature hysteresis width is broad compared with the 200 °C–grown film (see Fig. 3). We find that even the slight increase in T_G strongly affects the structural ordering and T_G of 200 °C is required for $B2$-ordered $Fe_{100-x}Rh_x$ films.

Next, we examine the effect of the postannealing on the $B2$-ordering for the RT-grown $Fe_{42}Rh_{58}$ films. When the annealing temperature (T_A) is 350 °C (blue triangles), the magnetization in a low-temperature regime is relatively reduced compared with the as-grown film (red circles). Since we could not observe marked changes in the structural quality near the Fe_3Si/Ge(111) interface and a large reduction in the magnetization for the Fe_3Si film after the postannealing at

T_A of 350 °C [39], the change in the M-T curve indicates the enhancement in the degree of the $B2$ ordering in the $Fe_{42}Rh_{58}$ film. After the postannealing at T_A of 400 °C (purple squares), on the other hand, a significant difference in the M-T curve is observed. The magnetization in a low-temperature regime is enhanced and that in a high-temperature regime is significantly reduced. The θ-2θ XRD patten of the sample annealed at T_A of 400 °C is also shown in the inset of Fig. 5. Some diffraction peaks originating from the formation of Rh- and Fe-based germinide compounds are seen (see arrows), implying the atomic interdiffusion in the $Fe_{42}Rh_{58}/D0_3$-Fe_3Si/Ge(111) by the postannealing. We can conclude that, for the RT-grown $Fe_{42}Rh_{58}$ films, postannealing at T_A of 350 °C can act effectively on the improvement of the structural ordering, but the quality of the annealed film is poor compared with the 200 °C–grown one.

It should be noted that 200 °C–grown $Fe_{100-x}Rh_x$ films, shown in Figs. 2 and 3, form $B2$-ordered structures even in as-grown conditions. The quality is comparable to that of the thin-film sample annealed at 600 °C reported [26] and the $B2$-ordering temperature is much lower than reported so far [3–37]. We speculate that the MBE process with Knudsen cells can achieve the homogeneous supply of Fe and Rh atoms on the surface of the $D0_3$-Fe_3Si buffer layer by accurately controlling the cell temperatures, leading to low-temperature $B2$ ordering of $Fe_{100-x}Rh_x$ films. Because the homogeneity of Fe and Rh atoms is not enough to form $B2$-ordered $Fe_{100-x}Rh_x$ at T_G of RT in the present growth condition, the increase in T_G from RT to 200 °C can act effectively for the formation of $B2$-ordered $Fe_{100-x}Rh_x$. In our opinion, if the local stoichiometry of Fe and Rh was improved in as-grown conditions, highly $B2$-ordered structures could be formed even at T_G of RT.

D. An all-epitaxial spin-valve structure

Recently, by using RT-MBE, we demonstrated an all-epitaxial pseudo-spin-valve structure, where it consists of ferromagnetic and nonmagnetic bcc alloys [48]. We consider that this result is also attributed to the atomic arrangement matching along ⟨111⟩. Finally, we try to demonstrate a spin-valve structure with an $Fe_{100-x}Rh_x$ AFM pinning layer. Before the growth of an $Fe_{42}Rh_{58}$ layer, we formed an all-epitaxial $Co_{60}Fe_{40}$(10 nm)/FeSi(10 nm)/Fe_3Si(10 nm) trilayer on Ge(111) at T_G of RT, where we co-evaporated each element with stoichiometry using Knudsen cells [48]. The growth rate for $Co_{60}Fe_{40}$ and FeSi was ∼1.7 nm/min and ∼1.0 nm/min, respectively [48]. The cell temperature of Co and Fe for the growth of $Co_{60}Fe_{40}$ was ∼1205 and ∼1200 °C and that of Fe and Si for FeSi was ∼1200 and ∼1380 °C. Observing the atomically smooth surface from *in situ* RHEED patterns, we grew a 100-nm-thick $Fe_{42}Rh_{58}$ layer at T_G of 200 °C. As a result, even on top of the trilayer, two-dimensional epitaxial growth was observed from *in situ* RHEED patterns (not shown).

Figure 6(a) shows a cross-sectional TEM image of the $Fe_{42}Rh_{58}$(100 nm)/$Co_{60}Fe_{40}$(10 nm)/FeSi(10 nm)/Fe_3Si (10 nm) spin-valve structure on Ge(111). From this image, we can identify successful growth of the all-epitaxial stacking structure. We also measured nanobeam electron diffraction (NED) patterns of each layer at points 1 through 4 denoted

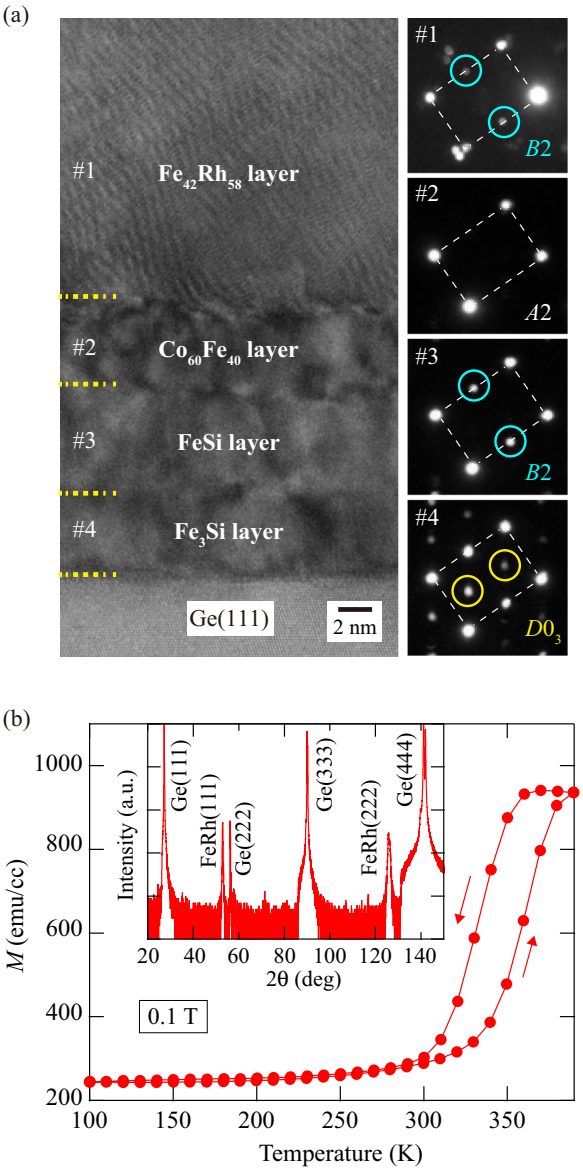

FIG. 6. (Color online) (a) Cross-sectional TEM image of $Fe_{42}Rh_{58}$(100 nm)/$Co_{60}Fe_{40}$(10 nm)/FeSi(10 nm)/Fe_3Si(10 nm) spin-valve structure on Ge(111) and NED patterns of each layer at points 1 through 4 denoted in the TEM image. (b) M-T curve of the sample. The inset shows θ-2θ XRD pattern of the sample.

in the TEM image. Each layer forms a bcc crystal structure and superlattice reflections resulting from the presence of $B2$-ordered $Fe_{42}Rh_{58}$ (point 1), $B2$-ordered FeSi (point 3), and $D0_3$-ordered Fe_3Si (point 4) are observed. The θ-2θ XRD pattern is shown in the inset of Fig. 6(b). Clear (111) and (222) diffraction peaks of $B2$-ordered $Fe_{100-x}Rh_x$ are seen, as discussed in Sec. III A. The M-T curve of the all-epitaxial stacking structure is shown in Fig. 6(b). We can see that the AFM-FM phase transition occurs above 300 K and a temperature hysteresis width of the AFM-FM phase transition is small. These features are quite similar to those of $Fe_{42}Rh_{58}$ films grown on top of a $D0_3$-Fe_3Si buffer layer on Ge(111) (see Fig. 3). Thanks to the low $B2$-ordering temperature, stacking $B2$-ordered $Fe_{42}Rh_{58}$ on top of a pseudo-spin-valve structure

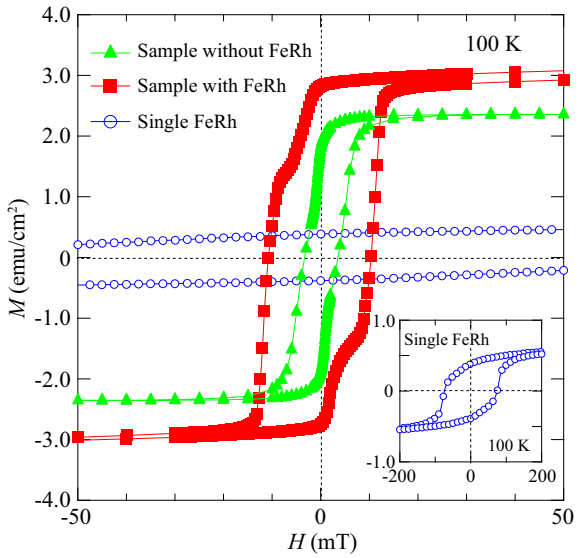

FIG. 7. (Color online) Low-field *M-H* curves at 100 K for sample without FeRh (green triangles), sample with FeRh (red squares), and single FeRh layer (blue circles). The inset shows a high-field *M-H* curve at 100 K for the single FeRh layer.

was demonstrated, meaning an achievement of the growth of $B2$-ordered $Fe_{42}Rh_{58}$ on top of other bcc-alloy-based buffer structures.

To evaluate magnetic properties of the spin-valve structure, we measured *M-H* curves at 100 K. For the measurement, the sample was first heated to 380 K under the application of a magnetic field of 9 T to align the magnetic moments of the FM $Fe_{42}Rh_{58}$ layer along the applied magnetic field, and then the sample was field-cooled down to 100 K and the magnetic field was removed. *M-H* curves for the $Fe_{42}Rh_{58}$(100 nm)/$Co_{60}Fe_{40}$(10 nm)/FeSi(10 nm)/Fe_3Si(10 nm) multilayer on Ge(111) (sample with FeRh) and the $Co_{60}Fe_{40}$ (10 nm)/FeSi(10 nm)/Fe_3Si(10 nm) trilayer on Ge(111) (sample without FeRh) are displayed in Fig. 7, together with that for $Fe_{42}Rh_{58}$(100 nm)/Fe_3Si(2 nm) layer on Ge(111) (single FeRh). The *M-H* curve for the sample without FeRh has a step, indicating that the top $Co_{60}Fe_{40}$ layer and the bottom Fe_3Si layer are magnetically decoupled by an FeSi spacer layer at 100 K. Since the coercivity of $Co_{60}Fe_{40}$ [49] is larger than that of Fe_3Si [39], the changes in the magnetization observed at ∼3.5 and ∼11 mT correspond to the magnetization switching fields of the Fe_3Si layer and the $Co_{60}Fe_{40}$ layer, respectively. It should be noted that the magnetization switching field of the $Co_{60}Fe_{40}$ layer for the sample with FeRh is markedly enhanced compared with the sample without FeRh. We speculate that this feature means the presence of the exchange coupling between FM $Co_{60}Fe_{40}$ layer and AFM $Fe_{42}Rh_{58}$ layer. However, the exchange coupling between FM $Co_{60}Fe_{40}$ layer and the FM component in the $Fe_{42}Rh_{58}$ layer should be taken into consideration because of the presence of the weak FM component at 100 K.

In Fig. 7 we measured a low-field *M-H* curve at 100 K for single FeRh (blue circles). Here a high-field *M-H* curve is also shown in the inset of Fig. 7. The *M-H* curve for the single FeRh has a low remanent magnetization (∼0.5 emu/cm^2) and a large coercivity (∼75 mT). Note that the magnitude of the magnetization of the single FeRh is comparable to the difference in the magnetization between the sample with FeRh and the sample without FeRh. The observed magnetization originates from a remaining FM component in the single FeRh, but it is quite smaller than the magnetization of the $Co_{60}Fe_{40}$ layer. On the other hand, the large coercivity of ∼75 mT could not be explained by the single FeRh because the ferromagnetic state (∼380 K) has a relatively small coercivity of ∼4 mT. Thus, the large coercivity of ∼75 mT is likely induced by the strong exchange coupling between FM and AFM components in the single FeRh at 100 K. Considering the large exchange coupling dominated by the AFM component, we infer that the ferromagnetic interaction between the FM component in the $Fe_{42}Rh_{58}$ layer and the $Co_{60}Fe_{40}$ layer is relatively weak compared to the exchange interaction between the dominant AFM $Fe_{42}Rh_{58}$ layer and the $Co_{60}Fe_{40}$ layer. Therefore, we can recognize that the coercivity of the $Co_{60}Fe_{40}$ layer is enhanced by the exchange interaction with the AFM $Fe_{42}Rh_{58}$ layer at 100 K.

Recently, Suzuki *et al.* reported that the exchange bias for Fe/FeRh(111) bilayers on Al_2O_3(0001) arises from the interface exchange coupling [31]. In this study, on the other hand, we could not observe a clear exchange bias for the spin-valve structure with the FeRh layer over the temperature region from 100 to 300 K. As described above, the presence of the FM component in the $Fe_{42}Rh_{58}$ layer might lead to a weak exchange bias at the $Fe_{42}Rh_{58}/Co_{60}Fe_{40}$ interface. Since the disordered $Fe_{42}Rh_{58}$ structures are induced by the lattice strain at the FeRh/FM interface [30,32], one should form a spin-valve structure consisting of a pinned FM layer with lattice matching.

IV. CONCLUSION

By using MBE with an insertion of a $D0_3$-Fe_3Si buffer layer, which has good atomic arrangement matching with $Fe_{100-x}Rh_x$ along ⟨111⟩, $B2$-ordered $Fe_{100-x}Rh_x$ films can be obtained at 200 °C even in as-grown conditions. We found that the disordered structures are easily formed near the interface between $Fe_{100-x}Rh_x$ and Fe_3Si because they are mainly derived from the the lattice strain in the $Fe_{100-x}Rh_x$ films due to the lattice mismatch. Since postannealing could not act effectively on the improvement of the degree of the $B2$ ordering in the $Fe_{100-x}Rh_x$ films, we proposed that it is important to explore the $B2$ ordering in as-grown conditions. The low-temperature $B2$ ordering of $Fe_{100-x}Rh_x$ films enabled us to form an all-epitaxial spin-valve structure consisting of bcc alloys, meaning that the $B2$-ordered $Fe_{100-x}Rh_x$ films can be obtained even on top of other bcc alloys.

ACKNOWLEDGMENTS

The authors would like to thank Professor M. Miyao of Kyushu University for useful discussion. This work was supported in part by JSPS KAKENHI Grants No. 26103003, No. 25246020, No. 26289229.

[1] M. Fallot and R. Hocart, Rev. Sci. **77**, 498 (1939).
[2] F. de Bergevin and L. Muldawer, C. R. Acad. Sci. **252**, 1347 (1961).
[3] J. S. Kouvel and C. C. Hartelius, J. Appl. Phys. **33**, 1343 (1962).
[4] M. R. Ibarra and P. A. Algarabel, Phys. Rev. B **50**, 4196 (1994).
[5] P. A. Algarabel, M. R. Ibarra, C. Marquina, A. d. Moral, J. Galibert, M. Iqbal, and S. Askenazy, Appl. Phys. Lett. **66**, 3061 (1995).
[6] S. Yuasa, M. Nyvlt, T. Katayama, and Y. Suzuki, J. Appl. Phys. **83**, 6813 (1998).
[7] S. Hashi, S. Yanase, Y. Okazaki, and M. Inoue, IEEE Trans. Magn. **40**, 2784 (2004).
[8] T. J. Zhou, K. Cher, J. F. Hu, Z. M. Yuan, and B. Liu, J. Appl. Phys. **111**, 07C116 (2012).
[9] X. Marti, I. Fina, C. Frontera, J. Liu, P. Wadley, Q. He, R. J. Paull, J. D. Clarkson, J. Kudrnovský, I. Turek, J. Kunes, D. Yi, J-H. Chu, C. T. Nelson, L. You, E. Arenholz, S. Salahuddin, J. Fontcuberta, T. Jungwirth, and R. Ramesh, Nat. Mater. **13**, 367 (2014).
[10] T. Naito, I. Suzuki, M. Itoh, and T. Taniyama, J. Appl. Phys. **109**, 07C911 (2011).
[11] R. O. Cherifi, V. Ivanovskaya, L. C. Phillips, A. Zobelli, I. C. Infante, E. Jacquet, V. Garcia, S. Fusil, P. R. Briddon, N. Guiblin, A. Mougin, A. A. Ünal, F. Kronast, S. Valencia, B. Dkhil, A. Barthélémy, and M. Bibes, Nat. Mater. **13**, 345 (2014).
[12] I. Suzuki, M. Itoh, and T. Taniyama, Appl. Phys. Lett. **104**, 022401 (2014).
[13] I. Radu, C. Stamm, N. Pontius, T. Kachel, P. Ramm, J.-U. Thiele, H. A. Dürr, and C. H. Back, Phys. Rev. B **81**, 104415 (2010).
[14] G. Shirane, C. W. Chen, P. A. Flinn, and R. Nathans, Phys. Rev. **131**, 183 (1963).
[15] P. H. L. Walter, J. Appl. Phys. **35**, 938 (1964).
[16] J. S. Kouvel, J. Appl. Phys. **37**, 1257 (1966).
[17] S. Yuasa, T. Akiyama, H. Miyajima, and Y. Otani, J. Phys. Soc. Jpn. **64**, 3978 (1995).
[18] R. Barua, F. Jiménez-Villacorta, and L. H. Lewis, Appl. Phys. Lett. **103**, 102407 (2013).
[19] Y. Ohtani and I. Hatakeyama, J. Appl. Phys. **74**, 3328 (1993).
[20] Y. Ohtani and I. Hatakeyama, J. Magn. Magn. Mater. **131**, 339 (1994).
[21] S. Yuasa, T. Katayama, K. Murata, M. Usukura, and Y. Suzuki, J. Magn. Magn. Mater. **177**, 1296 (1998).
[22] G. Ju, J. Hohlfeld, B. Bergman, R. J. M. van de Veerdonk, O. N. Mryasov, J.-Y. Kim, X. Wu, D. Weller, and B. Koopmans, Phys. Rev. Lett. **93**, 197403 (2004).
[23] S. Maat, J.-U. Thiele, and E. E. Fullerton, Phys. Rev. B **72**, 214432 (2005).
[24] B. Bergman, G. Ju, J. Hohlfeld, R. J. M. van de Veerdonk, J.-Y. Kim, X. Wu, D. Weller, and B. Koopmans, Phys. Rev. B **73**, 060407 (2006).
[25] C. Stamm, J.-U. Thiele, T. Kachel, I. Radu, P. Ramm, M. Kosuth, J. Minár, H. Ebert, H. A. Dürr, W. Eberhardt, and C. H. Back, Phys. Rev. B **77**, 184401 (2008).
[26] J. Cao, N. T. Nam, S. Inoue, H. Y. Y. Ko, N. N. Phuoc, and T. Suzuki, J. Appl. Phys. **103**, 07F501 (2008).
[27] Y. Ding, D. A. Arena, J. Dvorak, M. Ali, C. J. Kinane, C. H. Marrows, B. J. Hickey, and L. H. Lewis, J. Appl. Phys. **103**, 07B515 (2008).
[28] D. Kande, D. Laughlin, and J.-G. Zhu, J. Appl. Phys. **107**, 09E318 (2010).
[29] J.-S. Lee, E. Vescovo, L. Plucinski, C. M. Schneider, and C.-C. Kao, Phys. Rev. B **82**, 224410 (2010).
[30] I. Suzuki, T. Koike, M. Itoh, T. Taniyama, and T. Sato, J. Appl. Phys. **105**, 07E501 (2009).
[31] I. Suzuki, Y. Hamasaki, M. Itoh, and T. Taniyama, Appl. Phys. Lett. **105**, 172401 (2014).
[32] R. Fan, C. J. Kinane, T. R. Charlton, R. Dorner, M. Ali, M. A. de Vries, R. M. D. Brydson, C. H. Marrows, B. J. Hickey, D. A. Arena, B. K. Tanner, G. Nisbet, and S. Langridge, Phys. Rev. B **82**, 184418 (2010).
[33] D. W. Cooke, F. Hellman, C. Baldasseroni, C. Bordel, S. Moyerman, and E. E. Fullerton, Phys. Rev. Lett. **109**, 255901 (2012).
[34] A. X. Gray, D. W. Cooke, P. Krüger, C. Bordel, A. M. Kaiser, S. Moyerman, E. E. Fullerton, S. Ueda, Y. Yamashita, A. Gloskovskii, C. M. Schneider, W. Drube, K. Kobayashi, F. Hellman, and C. S. Fadley, Phys. Rev. Lett. **108**, 257208 (2012).
[35] K. M. Cher, T. J. Zhou, and J. S. Chen, IEEE Trans. Magn. **47**, 4033 (2011).
[36] G. C. Han, J. J. Qiu, Q. J. Yap, P. Luo, T. Kanbe, T. Shige, D. E. Laughlin, and J.-G. Zhu, J. Appl. Phys. **113**, 123909 (2013).
[37] S. Lounis, M. Benakki, and C. Demangeat, Phys. Rev. B **67**, 094432 (2003).
[38] K. Hamaya, Y. Ando, T. Sadoh, and M. Miyao, Jpn. J. Appl. Phys. **50**, 010101 (2011).
[39] K. Hamaya, T. Murakami, S. Yamada, K. Mibu, and M. Miyao, Phys. Rev. B **83**, 144411 (2011).
[40] S. Yamada, J. Sagar, S. Honda, L. Lari, G. Takemoto, H. Itoh, A. Hirohata, K. Mibu, M. Miyao, and K. Hamaya, Phys. Rev. B **86**, 174406 (2012).
[41] I. Galanakis, P. H. Dederichs, and N. Papanikolaou, Phys. Rev. B **66**, 174429 (2002).
[42] R. Shan, H. Sukegawa, W. H. Wang, M. Kodzuka, T. Furubayashi, T. Ohkubo, S. Mitani, K. Inomata, and K. Hono, Phys. Rev. Lett. **102**, 246601 (2009).
[43] R. Farshchi and M. Ramsteiner, J. Appl. Phys. **113**, 191101 (2013).
[44] T. Kimura, N. Hashimoto, S. Yamada, M. Miyao, and K. Hamaya, NPG Asia Mater. **4**, e9 (2012); K. Hamaya, N. Hashimoto, S. Oki, S. Yamada, M. Miyao, and T. Kimura, Phys. Rev. B **85**, 100404(R) (2012).
[45] S. Yamada, K. Tanikawa, M. Miyao, and K. Hamaya, Cryst. Growth Des. **12**, 4703 (2012).
[46] M. Kawano, S. Yamada, K. Tanikawa, K. Sawano, M. Miyao, and K. Hamaya, Appl. Phys. Lett. **102**, 121908 (2013).
[47] F. Stromberg, S. Bedanta, C. Antoniak, W. Keune, and H. Wende, J. Phys.: Condens. Matter. **20**, 425205 (2008).
[48] J. Hirayama, K. Tanikawa, M. Kawano, S. Yamada, M. Miyao, and K. Hamaya, IEEE Trans. Magn. **50**, 11 (2014).
[49] Y. Maeda, K. Hamaya, S. Yamada, Y. Ando, K. Yamane, and M. Miyao, Appl. Phys. Lett. **97**, 192501 (2010).